Mon. Not. R. Astron. Soc. **000**, 000–000 () Printed 10 March 2011 (MN LATEX style file v2.2)

Type Ia supernova diversity: white dwarf central density as a secondary parameter in three-dimensional delayed detonation models

I. R. Seitenzahl[1], F. Ciaraldi-Schoolmann[1], F. K. Röpke[1]
[1] *Max-Planck-Institut für Astrophysik, 85741 Garching, Germany*

10 March 2011

ABSTRACT

Delayed detonations of Chandrasekhar-mass white dwarfs (WDs) have been very successful in explaining the spectra, light curves, and the width-luminosity relation of spectroscopically normal Type Ia supernovae (SNe Ia). The ignition of the thermonuclear deflagration flame at the end of the convective carbon "simmering" phase in the core of the WD is still not well understood and much about the ignition kernel distribution remains unknown. Furthermore, the central density at the time of ignition depends on the still uncertain screened carbon fusion reaction rates, the accretion history and cooling time of the progenitor, and the composition. We present the results of twelve high-resolution three-dimensional delayed detonation SN Ia explosion simulations that employ a new criterion to trigger the deflagration to detonation transition (DDT). The simulations fall into into three ignition categories: relatively bright SNe with 5 ignition kernels and a weak deflagration phase (three different central densities), relatively dim SNe with 1600 ignition kernels and a strong deflagration phase (three different central densities) and intermediate SNe with 200 ignition kernels (six different central densities). All simulations trigger our DDT criterion and the resulting delayed detonations unbind the star. We find a trend of increasing iron group element (IGE) production with increasing central density for all three categories. The total ^{56}Ni yield, however, remains more or less constant, even though increased electron captures at high density result in a decreasing ^{56}Ni mass fraction of the IGE material. We attribute this to an approximate balance of ^{56}Ni producing and destroying effects. The deflagrations that were ignited at higher density initially have a faster growth rate of subgrid-scale turbulence. Hence, the effective flame speed increases faster, which triggers the DDT criterion earlier, at a time when the central density of the expanded star is higher. This leads to an overall increase of IGE production, which off-sets the percental reduction of ^{56}Ni due to neutronization.

Key words: nuclear reactions, nucleosynthesis, abundances – supernovae: general

1 INTRODUCTION

SNe Ia have come to fame as the Universe's most luminous standardizable candles – crucial ingredients to the study of dark energy and cosmology (e.g. Riess et al.1998; Schmidt et al. 1998). A limiting factor on the precision of using SNe Ia as distance indicators is the inherent scatter in their normalized light curves (e.g. Wood-Vasey et al. 2007). A better understanding of the intrinsic variation of supernova brightnesses and spectra is needed (e.g. Albrecht et al. 2006; Miknaitis 2007). Simulations of SN Ia explosions are already being used to aid in improving the precision of cosmological distance measurements based on supernovae in the future (e.g. Blondin et al. 2011). In addition, SNe Ia also play a critical role in galaxy gas kinematics (e.g. Scannapieco et al. 2008), positron production (e.g. Chan & Lingenfelter 1993), and chemical evolution (e.g. Matteucci & Greggio 1986). Detailed modeling of the explosions is therefore useful for understanding the origin of the Galactic 511 keV line, the origin and evolution of heavy elements, and kinetic supernova feedback, and measuring the Hubble parameter as a function of redshift. The standard model of SNe Ia relies on the nuclear fusion of the initial composition (predominantly ^{12}C and ^{16}O) of a massive white dwarf (WD) star to more tightly bound nuclei to power the explosion (Hoyle & Fowler 1960). The exact nature of the progenitor systems and de-

tails of the dynamics of the nuclear burning processes however are not known. Among the leading scenarios are the Chandrasekhar-mass models, in which a WD accretes matter from a companion star and grows in mass to near the Chandrasekhar limit until pycnonuclear carbon fusion reactions (Cameron 1959) start taking place. Once carbon fusion reactions produce more energy than is carried away by neutrino losses, the core becomes convective and when the nuclear burning time of a fluid element becomes shorter than the eddy turnover time a deflagration flame may be born (e.g. Woosley 1990). Numerical simulations of the convective stage leading up to the ignition of the deflagration were performed by Höflich & Stein (2002), Kuhlen et al. (2006), Piro & Chang (2008), Piro & Bildsten (2008), and Zingale et al. (2009). The central density of the WD decreases significantly during the simmering phase between the onset of carbon burning and the ignition of the deflagration (e.g. Lesaffre et al. 2006; Piro & Bildsten 2008). Those calculations, however, are not taking electron captures and the URCA process correctly into account, and some uncertainty in the evolution remains. The rate of the screened ^{12}C–^{12}C fusion reaction is still quite uncertain (e.g. Itoh et al. 2003; Jiang et al. 2007; Gasques et al. 2005, 2007). The central density at the time of ignition, however, depends only mildly on the exact value of this reaction rate (Cooper et al. 2009; Iapichino & Lesaffre 2010). More important is the initial mass and the accretion and cooling history of the WD, which determines the thermodynamic state of the interior. This results in a range of possible central densities at ignition, from less than 2×10^9 to over 5×10^9 g cm^{-3} (Lesaffre et al. 2006).

Metallicity has a considerable impact on the supernova brightness (e.g. Timmes et al. 2003; Travaglio et al. 2005; Bravo et al. 2010). In contrast, the ignition density has been shown to depend rather weakly on metallicity and the CO ratio (Lesaffre et al. 2006). If the initial deflagration flame can transition into a detonation (e.g. Khokhlov et al. 1997; Röpke 2007; Woosley 2007; Woosley et al. 2009), then good agreement of the models with observations can be obtained (e.g. Röpke & Niemeyer 2007; Bravo & García-Senz 2008; Kasen et al. 2009). A successful explosion model has to reproduce the observed range of peak absolute magnitudes (i.e. ^{56}Ni masses) and the width-luminosity relation and scatter thereabout. Furthermore, the observed correlation between the brightness of an event and the delay time or age of the host stellar population has to be explained (e.g. Gallagher et al. 2008). Recently, a connection between age of the host stellar population and SN Ia brightness was proposed via the effect of longer cooling times on the ignition density (Krueger et al. 2010). Varying the central density for 150 two dimensional delayed detonation supernova simulations within the statistical ignition framework presented in Townsley et al. (2009), the authors found that the ^{56}Ni yield decreased with increasing central density, while the total iron group element (IGE) yield remains roughly constant. This is attributed to increased production of stable isotopes (such as e.g. ^{54}Fe or ^{58}Ni) due to increased neutronization via electron captures at the higher densities. There are, however, at least three competing effects that influence the ^{56}Ni mass produced in a delayed detonation SN.

(i) Electron capture rates on protons and iron-group isotopes under electron degenerate condisitons are strongly increasing with density (e.g. Langanke & Martínez-Pinedo 2001). Consequently, a distribution of nuclei in nuclear statistical equilibrium at high density neutronizes at a much faster rate than one at lower density (e.g. Seitenzahl et al. 2009), which acts to lower the ^{56}Ni mass.

(ii) Near Chandrasekhar-mass WDs in hydrostatic equilibrium with a higher central density are more compact, i.e. significantly smaller and slightly more massive and tighly bound. This may translate into a more compact WD at the time of the first DDT, which could lead to an overall larger part of the WD being burned to IGEs, which acts to raise the ^{56}Ni mass.

(iii) Deflagrations evolve differently at higher gravitational acceleration g (Khokhlov 1995; Zhang et al. 2007). From linear stability analysis, the Rayleigh-Taylor temporal growth rate scales with $\sqrt{g}$. The different flame evolution and turbulence generation could have an effect on the DDT (e.g. the transition density), which, depending on the different degree of "pre-expansion", could either lower or raise the ^{56}Ni mass.

The effect of variations in the central density of the WD on *pure deflagrations* has been explored in three-dimensional models before (Röpke et al. 2006). Here, we present the results of twelve high-resolution three-dimensional *delayed detonation* SN Ia simulations (that employ a new DDT criterion, see Section 2.3) for three different ignition configurations and a range of central densities. We find that, for the same spatial ignition spark distributions, the ^{56}Ni yield remains more or less constant a function of central density at ignition. The deflagrations that were ignited at higher density produce subgrid-scale turbulence at a higher rate, which triggers the DDT criterion earlier when the central density of the star is higher. This leads to an overall increase of IGE production as well as enhanced electron captures. Even though the mass in ^{56}Ni comprises a smaller fraction of the mass that has burned to IGEs, the overall ^{56}Ni yield remains roughly constant since more total mass in IGEs is produced in the detonation. Only the cases where much of the IGEs are produced in the deflagration phase show a trend of decreasing ^{56}Ni with central density. In Section 2 we introduce our setup and briefly review the computational methods, in Section 3 and 4 we present and discuss the results, and in Section 5 we conclude.

2 METHODS AND SIMULATIONS

The large computational demands of the high-resolution three- dimensional simulations we perform prevented a statistical framework approach similar to the one presented in Townsley et al. (2009), Krueger et al. (2010) and Jackson et al. (2010). Under the constraints of limited computational resources, we chose six different densities for a setup with an intermediate number of ignition points (200 kernels), and three densities each for the setups with the least (5 kernels) and the most (1600 kernels) ignition points respectively. The central densities are such that they cover the distribution of ignition densities expected from different cooling ages and accretion histories Lesaffre et al. (2006). The ignition spark configurations are selected in a way that SNe with a range of brightnesses with ^{56}Ni masses between ~ 0.45 and 1.1 M$_\odot$ are obtained.

2.1 Initial models

All simulations presented here are full star simulations performed in 3D. The initial stellar models are cold, isothermal ($T = 5 \times 10^5$ K) WDs in hydrostatic equilibrium with central density ρ_c ranging from 1.0 to 5.5×10^9 g cm^{-3}. The composition is assumed to be 47.5 per cent ^{12}C, 50 per cent ^{16}O, and 2.5 per cent ^{22}Ne (to account for solar metallicity of the zero-age main-sequence progenitor) by mass homogeneously throughout the star, resulting in an electron fraction $Y_e = 0.49886$.

A strong deflagration phase leads to more energy release and hence expansion of the star. The ensuing detonation then produces less ^{56}Ni, leading to a dimmer event. In the multi-spot ignition scenarios, the strongest deflagrations are obtained by placing an optimal number of ignition sparks approximately symmetrically about the center (García-Senz & Bravo 2005; Livne et al. 2005; Röpke et al. 2007). While too few ignition sparks lead to an overall weak deflagration, too many of them lead to vigorous burning in the initial stage and thus an early expansion of the WD that suppresses burning in later stages of the deflagration (Röpke et al. 2006).

Asymmetric ignition spark distributions lead to a weaker deflagration phase and hence a brighter SN Ia (Röpke et al. 2007; Kasen et al. 2009). For the ignition of the deflagration we use setups generated from a Monte-Carlo based algorithm. The primary input parameters are the number of the ignition kernels and the distribution type. The details of the ignition process remain unknown. Woosley et al. (2004) and Wunsch & Woosley (2004) conclude from analytical models that multi-spot ignition within the inner ∼150 km or so is a possible scenario. The total number and spatial distribution of the ignition spots, however, was not conclusively constrained by their models. We investigate three different sets of explosion models corresponding to different ignition scenarios. We choose configurations of 5, 200, and 1600 kernels which are spherically arranged around the center of the WD following a Gaussian distribution in radius. The placement of kernels with a distance greater than 2.5 times than a given variance σ is suppressed. For the setups with 5, 200, and 1600 kernels, we set $\sigma = 0.6$, 0.75, and 1.8×10^7 cm, respectively. The radius of the spherical ignition kernels is set to $R_k = 10^6$ cm. Finally, we impose a length scale D_k, which the distances between the centers of the ignition kernels have to exceed. D_k is set to 10^6, 3×10^5, and 5×10^4 cm for the setups with 5, 200, and 1600 kernels, respectively. Note that for $R_k > D_k$, the sparks may partially overlap which is the case for the setups with 200 and 1600 kernels. Within a given model suite (i.e. 5, 200, or 1600 kernels), the locations of the ignition sparks are only once randomly determined in the beginning; the resulting spatial realization of the ignition configuration is then kept fixed and identical in all the simulations with different central density. With these choices of ignition spark distributions we cover a large range of ^{56}Ni masses, between ~ 0.45 and 1.1 $M_\odot$, which is consistent with normal SNe Ia (e.g. Contardo et al. 2000; Stritzinger et al. 2006a,b).

2.2 Computational method

The reactive Euler equations are solved using a finite volume scheme based on the PROMETHEUS code by Fryxell et al. (1989), which is an implementation of the "piecewise parabolic method" (PPM) of Colella & Woodward (1984). The grid resolution is $512 \times 512 \times 512$ cells for all simulations. We use the expanding hybrid grid implementation of Röpke & Hillebrandt (2005a,b), with a uniform inner grid that contains the deflagration level set and a non-uniform outer grid that covers the remainder of the computational domain. Our simulation code is based on a large eddy simulation (LES) approach, which resolves the largest turbulent structures and models the turbulence on unresolved scales using a turbulence subgrid-scale model (for details see Schmidt et al. 2006a,b). The code uses a comoving grid (Röpke 2005; Röpke et al. 2006) with an outer coarse grid following the WD's expansion and an inner finer grid tracking the flame front. The flame itself is treated as a discontinuity separating fuel and ash; its propagation is tracked with the level set technique (Osher & Sethian 1988; Smiljanovski et al. 1997; Reinecke et al. 1999). In this thin flame approximation, the energy liberated in the nuclear burning is released immediately behind the level set representing the flame surface. Since nuclear matter burned in a deflagration undergoes different burning than matter processed in a detonation, separate level-set representations are used (Golombek & Niemeyer 2005; Röpke & Niemeyer 2007). Using a full nuclear reaction network in every computional cell to calculate the source terms for the hydrodynamics is currently still computationally too expensive for three-dimensional simulations. We solve this problem by tabulating the energy release as a function of fuel density. For the detonation we use the new tables from Fink et al. (2010). A table for the energy release of the deflagration level set was calculated in a similar way.

2.3 DDT criterion

The transition from a subsonic deflagration to a supersonic detonation based on the Zel'dovich gradient mechanism (Zel'dovich et al. 1970) was introduced to SN Ia theory by Blinnikov & Khokhlov (1986) and further analyzed by Khokhlov (1991a,b); Khokhlov et al. (1997) and Niemeyer & Woosley (1997). The main result of their studies was that such a transition is only possible in the turbulent deflagration stage, where large velocity fluctuations v' lead to a mixing of cold fuel and hot ash up to a certain length scale. These "hot spots" are supposed to be the seeds of a DDT. Lisewski et al. (2000) pointed out that v' must exceed 10^8 cm s^{-1}. Indeed, velocity fluctuations on this scale have already been found in three-dimensional deflagration simulations (Röpke 2007). Woosley (2007) argued that for DDTs there are specific restrictions on the burning properties deep in the distributed burning regime, which is the regime where strong turbulent flame interactions are expected. As DDTs cannot be resolved in full-star simulations, we employ a subgrid-scale model to calculate the probability of these transitions.

The details of this subgrid-scale DDT model, which is guided by the latest studies of the microscopic mechanism of DDTs in SNe Ia Woosley et al. (2009), are described in a

separate paper (Ciaraldi-Schoolmann & Röpke, in preparation). It accounts for the intensity of the turbulent velocity fluctuations as well as the fuel density $\rho_{\rm fuel}$ and fuel fraction $X_{\rm fuel}$ in the grid cells crossed by the flame front. If the probability $P(v' > v'_{\rm crit})$ to find velocity fluctuations larger then $v'_{\rm crit}$ in a specific area $A_{\rm flame}$ at the flame front exceeds a certain threshold $A_{\rm crit}$, detonations are ignited in the grid cells which contain the largest velocity fluctuations. $A_{\rm flame}$ is defined as the part of the flame where $\rho_{\rm fuel} = [0.6 - 0.8] \cdot 10^7$ g cm^{-3} and $X_{\rm fuel} = [0.3 - 0.7]$. To properly estimate this area, we take the fractal dimension of the flame front into account, which is ~ 2.36 (Sreenivasan 1991; Kerstein 1988; Woosley 2007). The number of ignitions is given by the ratio $A_{\rm flame}$ to $A_{\rm crit}$. The criterion must hold at least for half of an eddy turn $\tau_{\rm eddy_{1/2}} = L/V(L)$, where L is the turbulent integral scale and $V(L)$ the velocity at this scale. Following considerations of Woosley (2007), Ciaraldi-Schoolmann et al. (2009) and Röpke (2007) we assume $L = 10^6$ cm and $V(L) \approx [10^7 - 10^8]$ cm s^{-1}. We choose a constant value of $\tau_{\rm eddy_{1/2}} = 0.005$ s in our analysis. We further follow Lisewski et al. (2000) and Röpke (2007) and define $v'_{\rm crit} = 10^8$ cm s^{-1} and $A_{\rm crit} = 10^{12}$cm^2 as our thresholds for the DDT-criterion. While the details of the implementation are beyond the scope of this publication and will be presented elsewhere, we point out that this modeling approach is significantly different from simply fixing a certain DDT threshold density. Our criterion in addition requires strong local turbulent velocities. It is thus more restrictive and substantially reduces the number of DDTs.

3 RESULTS

The chosen distinct setups lead to different evolutions of the deflagration flame. In turn, the different evolutions of the flame front has great impact of the properties of the following delayed detonations (see Fig. 1).

On the one hand, the energy released during the deflagration stage up to the time $t_{\rm DDT}$ when the first DDT occurs, is smaller for simulations starting with fewer ignition kernels (see Table 1). The ensuing weaker expansion manifests itself in a higher central density at $t = t_{\rm DDT}$. This in turn translates into a larger fraction of the total mass of the WD burned into IGE during the detonation phase (see Table 2) than for the models with more ignition kernels. We thereby confirm that the strength of the deflagration is a primary parameter for the ^{56}Ni production (Röpke & Niemeyer 2007), and hence brightness, of a supernova that explodes in the delayed detonation scenario (see Fig. 2). A strong deflagration results in fainter events, primarily due to the large expansion of the star prior to the DDT, but also due to the copious neutronization in the deflagration phase (see Fig. 3).

On the other hand, for an identical spatial distribution of ignition kernels, the simulations with higher initial central density exhibit stronger turbulence production and the subgrid-scale energy grows at a faster rate initially (see Fig. 4). This can be understood by the difference in gravitational acceleration g. For the same *spatial* distribution of ignition spots, the distribution in the *mass* coordinate will be centered further out at larger mass and thus larger g in the higher central density case. For Rayleigh-Taylor dominated deflagration flames the turbulent burning velocity scales with $\sqrt{g}$ (e.g. Khokhlov 1995). Consequently, at equal time after ignition (e.g. 0.3s), a high central density model will have burned significantly more mass than a low central density model (compare Figs. 1b and 1c). As a further consequence, the higher the initial central density, the sooner our DDT criterion is fulfilled (see Table 1, but note the outlier with 5 ignition kernels for $\rho_{\rm c} = 3.5 \times 10^9$ g cm^{-3}). Importantly, there is a trend that models with high initial central density also have a higher central density at $t = t_{\rm DDT}$, which is a proxy for the amount of fuel at densities high enough that it will be burned to IGE in the detonation. We find

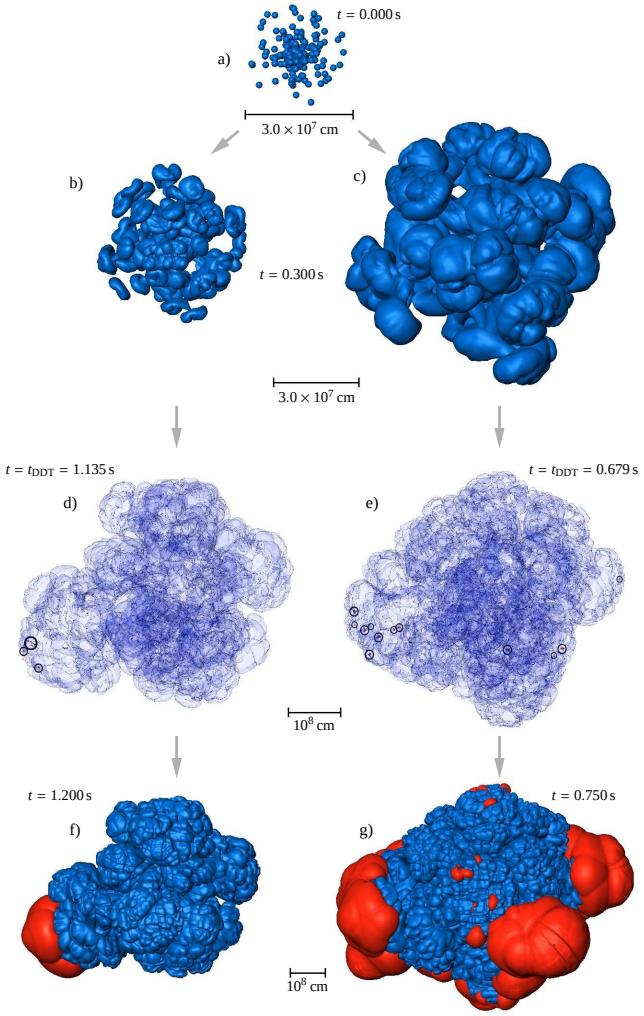

Figure 1. Shown are snapshots of the deflagration level set (blue) and the detonation level set (red) for the lowest (left column, $\rho_{\rm c} = 1.0 \times 10^9$ g cm^{-3}) and the highest (right column, $\rho_{\rm c} = 5.5 \times 10^9$ g cm^{-3}) central density. a) Both simulations initially have a spatially identical arrangement of the 200 ignition kernels. b/c) After $t = 0.3$s, the deflagration has burned significantly more for the high density case. d/e) The spots where the DDT criterion is first triggered are circled; the detonation triggers at an earlier time for the high density case. f/g) The detonation level set is propagating through unburned fuel away from the DDT spots. Multiple detonations can be launched as long as the DDT criterion is fulfilled. In spite of the differences in time evolution and morphology, both models produce the same amount of ^{56}Ni.

Table 1. DDT attributes for all models. Tabulated are the nuclear energy released $E_{\rm nuc}$, the central density $\rho_{\rm c}$, and the (average) density of the first DDT spot(s) $\bar{\rho}_1(t = t_{\rm DDT})$ at the time t_{DDT} when the first DDT(s) occured.

Model	$\rho_{\rm c}(t=0)$ [10^9 g cm^{-3}]	$t_{\rm DDT}$ [s]	$E_{\rm nuc}(t=t_{\rm DDT})$ [10^{51} ergs]	$\rho_{\rm c}(t=t_{\rm DDT})$ [10^8 g cm^{-3}]	$\bar{\rho}_1(t=t_{\rm DDT})$ [10^7 g cm^{-3}]
0005	1.5	1.253	0.334	4.911	0.773
...	3.5	0.890	0.246	11.610	0.758
...	5.5	0.911	0.488	6.183	0.716
0200	1.0	1.135	0.587	1.450	0.700
...	1.5	0.993	0.667	1.706	0.746
...	2.9	0.802	0.803	2.270	0.756
...	3.5	0.756	0.838	2.533	0.749
...	4.0	0.755	0.936	2.193	0.759
...	5.5	0.679	0.930	2.711	0.761
1600	1.5	1.077	0.813	0.718	0.705
...	3.5	0.848	0.990	0.827	0.779
...	5.5	0.757	1.087	0.875	0.755

Table 2. Nucleosynthetic yields for all models. Tabulated are the total WD mass $M_{\rm tot}$, and the final masses of ^{12}C, ^{16}O, intermediate mass elements, iron group elements, and ^{56}Ni ($M_{^{12}\rm C}$,$M_{^{16}\rm O}$,$M_{\rm IME}$,$M_{\rm IGE}$, and $M_{^{56}\rm Ni}$). Furthermore tabulated are the masses of iron group elements and ^{56}Ni at the time $t_{\rm DDT}$ when the first DDT(s) occured ($M^{\rm def}_{IGE}$ and $M^{\rm def}_{^{56}\rm Ni}$), as well as their respective relative fractions of the final masses, ($\frac{M^{\rm def}_{\rm IGE}}{M_{\rm IGE}}$ and $\frac{M^{\rm def}_{^{56}\rm Ni}}{M_{^{56}\rm Ni}}$).

Model	$\rho_{\rm c}(t=0)$ [10^9 g cm^{-3}]	$M_{\rm tot}$ [M$_\odot$]	$M_{^{12}\rm C}$ [M$_\odot$]	$M_{^{16}\rm O}$ [M$_\odot$]	$M_{\rm IME}$ [M$_\odot$]	$M_{\rm IGE}$ [M$_\odot$]	$M_{^{56}\rm Ni}$ [M$_\odot$]	$M^{\rm def}_{\rm IGE}$ [M$_\odot$]	$M^{\rm def}_{^{56}\rm Ni}$ [M$_\odot$]	$\frac{M^{\rm def}_{\rm IGE}}{M_{\rm IGE}}$	$\frac{M^{\rm def}_{^{56}\rm Ni}}{M_{^{56}\rm Ni}}$
0005	1.5	1.378	0.004	0.033	0.205	1.136	1.033	0.221	0.182	0.19	0.176
...	3.5	1.406	0.002	0.017	0.100	1.287	1.139	0.168	0.125	0.13	0.110
...	5.5	1.416	0.002	0.015	0.098	1.301	1.095	0.288	0.172	0.22	0.157
0200	1.0	1.361	0.017	0.104	0.447	0.793	0.698	0.385	0.321	0.49	0.460
...	1.5	1.378	0.012	0.073	0.390	0.904	0.768	0.447	0.348	0.49	0.453
...	2.9	1.400	0.008	0.063	0.346	0.984	0.752	0.547	0.359	0.56	0.477
...	3.5	1.406	0.006	0.053	0.307	1.040	0.770	0.573	0.354	0.55	0.460
...	4.0	1.409	0.007	0.057	0.314	1.031	0.735	0.622	0.375	0.60	0.510
...	5.5	1.416	0.007	0.053	0.280	1.076	0.698	0.626	0.325	0.58	0.466
1600	1.5	1.378	0.014	0.104	0.523	0.737	0.606	0.478	0.366	0.65	0.604
...	3.5	1.406	0.015	0.098	0.479	0.814	0.535	0.600	0.346	0.74	0.647
...	5.5	1.416	0.015	0.094	0.449	0.858	0.463	0.665	0.310	0.78	0.670

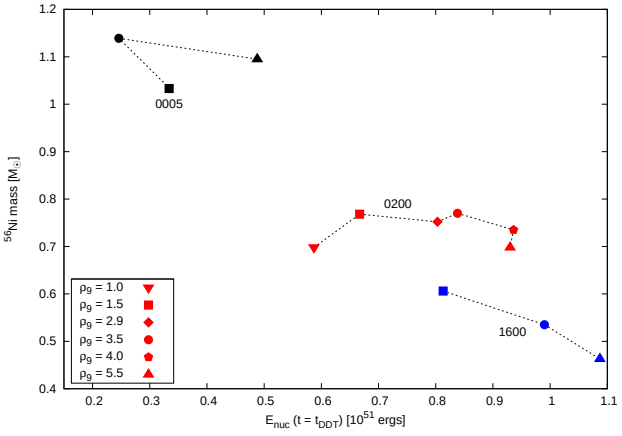

Figure 2. Shown is the mass of ^{56}Ni produced in the different explosions as a function of the total nuclear energy liberated during the deflagration phase up to $t = t_{\rm DDT}$.

that for all ignition kernel distributions, the total yield of IGE material within an ignition distribution suite increases with $\rho_{\rm c}$ (see Fig. 5 and Table 2). The total yield of ^{56}Ni appears flat with $\rho_{\rm c}$ for the model suites with 5 and 200 ignition kernels; only the model suite with the strongest deflagration phase (1600 ignition kernels) has a trend of decreasing ^{56}Ni with $\rho_{\rm c}$ (see Fig. 6 and Table 2).

4 DISCUSSION

We attribute the almost constant ^{56}Ni mass to a coincidental balance of the competing effects presented in Section 1, – the larger electron capture rates at higher central density are offset by a greater total mass in IGE due to the inherent compactness of the WD and faster evolution of the flame towards DDT. The high density simulations with 5 and 200 ignition sparks exhibit more subgrid-scale energy generation at early times and therefore higher flame speeds

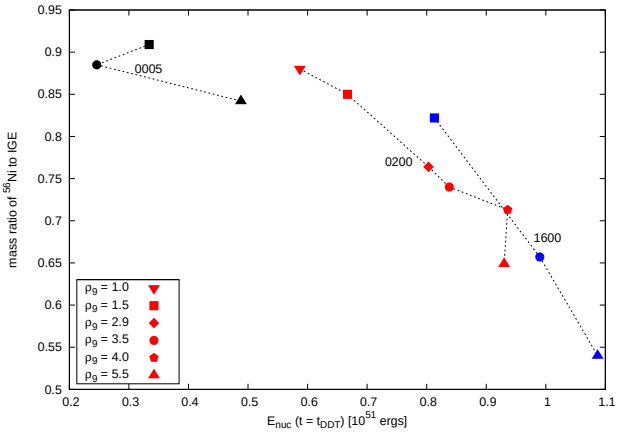

Figure 3. Shown is the relative mass fraction of ^{56}Ni to IGE produced in the different explosions as a function of the total nuclear energy liberated during the deflagration phase up to $t = t_{\rm DDT}$. It is evident that the strength of the deflagration (as measured by $E_{\rm nuc}(t = t_{\rm DDT})$) is a very good proxy for the mass ratio of ^{56}Ni to IGE.

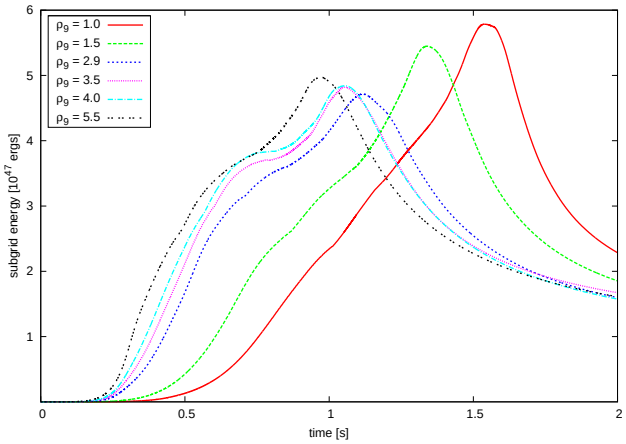

Figure 4. Shown is the subgrid-scale turbulent energy as a function of time for the model sequence with 200 ignition kernels. Note that the rate of turbulent energy production is initially larger for the high density cases.

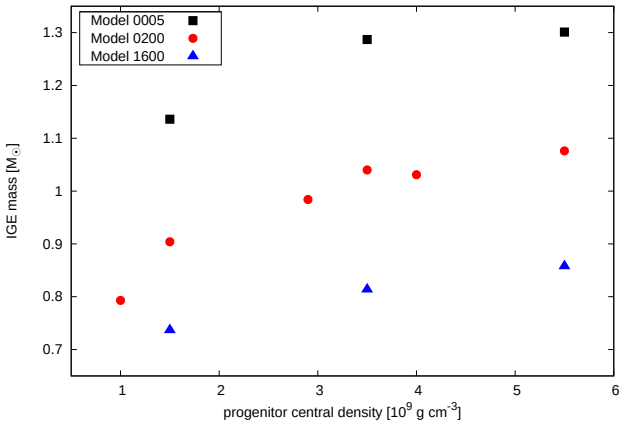

Figure 5. Shown is the mass of IGE as a function of central density $\rho_{\rm c}$ of the WD at the time the deflagration was ignited. A trend with increasing IGE mass with central density is evident for all three ignition configurations.

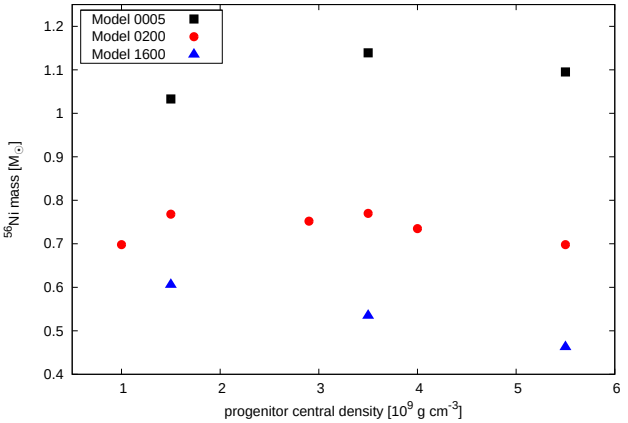

Figure 6. Shown is the mass of ^{56}Ni as a function of $\rho_{\rm c}(t = 0)$. Evidently, for these simulations the ignition configuration is the primary parameter that determines the ^{56}Ni mass (and hence peak brightness) of the events, whereas the central density is merely a secondary parameter.

initially. The still highly turbulent deflagration flame reaches the outer layers of the WD with low fuel density faster, and, consequently, the DDT criterion triggers earlier when the central density of the star is still higher (see Table 1). As a result, these simulations produce more IGE and even though the ^{56}Ni fraction of the IGEs is lower due to increased neutronization, (see Fig. 3), the total amount of ^{56}Ni remains roughly constant. The difference between ^{56}Ni and IGE is mainly made up of stable iron group nuclides such as ^{58}Ni, ^{54}Fe, but also other radioactive nuclides such as ^{57}Ni or ^{55}Co contribute.

The model suite with 1600 ignition kernels, which has such a high density of ignition sparks that the whole central region is filled with burning products of the deflagration, behaves differently. Due to the numerous ignition sites, a large part of central mass of the star is already burned in the deflagration before the first DDT occurs. The IGE produced in the deflagration, where most of the electron captures occur, are a large fraction of the total IGE produced (see Table 2). The electron captures and resulting shift of ^{56}Ni toward more neutron rich stable Fe-group isotopes occur most copiously behind the slowly moving deflagration flame front, and consequently the increased production of IGE material does not reflect in larger ^{56}Ni masses for cases where the deflagration contributes most of the IGE mass. The strong deflagration and vigorous expansion leads to such low central densities at $t = t_{\rm DDT}$ that the ensuing detonation cannot produce sufficient ^{56}Ni to counter this trend. Events producing such large amounts of strongly neutronized IGE matter cannot, however, make up most SN Ia events, due to the unusual isotopic composition (e.g. Woosley 1997).

We can only speculate why our simulations predict increasing IGE and roughly constant ^{56}Ni production for higher initial central density, whereas Krueger et al. (2010) find the opposite – decreasing ^{56}Ni and constant IGE. One possible reason for the different trends between the two sets of simulations is the way the DDT is handled.

For simulations of delayed detonations in SNe occurring via a DDT, the detonation is generally put in "by hand" (e.g. Arnett & Livne 1994; Livne 1999; Gamezo et al. 2005; Bravo & García-Senz 2008; Krueger et al. 2010) , usually by choosing a critical density where a deflagration transitions to a detonation. Recently, Jackson et al. (2010) investigated the effect the particular choice of such a transition density has. They found a quadratic dependence of the IGE yield on the log of the transition density. Instead of imposing a fixed transition density, we utilize a dynamic DDT criterion (see Section 2.3), which takes the effects of different deflagration evolutions on the detonation initiation into account. We point out that typical densities where our DDT criterion triggers (see Table 1) are lower than 10^7 g cm^{-3}. Jackson et al. (2010) have shown that the variance of the ^{56}Ni yield for a statistical set of simulations is relatively large for such a low choice of transition density (see figure 3 from their work), in agreement with our observed large range of ^{56}Ni masses obtained. Numerous other obvious differences between the simulation sets exist, including the nature of the propagation and the nuclear energy release of the burning fronts (level sets vs. reaction progress variables), the dimensionality of the simulations (3D vs 2D), or the structure of the computational mesh (AMR vs. expanding grid).

In this context, note the work of Meakin et al. (2009), who present a suite of supernova explosion models with different off-sets for the initial deflagration bubble. Although their single bubble off center ignition scenario does not explore central density at the time of the ignition of the deflagration as a parameter, their result that a strong deflagration phase need not necessarily result in less ^{56}Ni produced is the same. They also find that the total amount of IGE decreases for models that had a more vigorous deflagration phase (leading to more expansion) before the detonation is triggered, but the ^{56}Ni yields remains approximately constant (see figure 12 of their work).

5 CONCLUSIONS

We have performed twelve three-dimensional hydrodynamical simulations for delayed detonation SNe Ia for a range of central densities and ignition conditions. We find a trend of increasing IGE production with central density within each set of ignition conditions. This is because the high central density WDs are more compact and the flame evolves faster; the DDT occurs sooner when more unburned material is still above the density threshold ($\approx 10^7$ g cm^{-3}) where a detonation will still produce IGE. In spite of the larger IGE mass, the more vigorous neutronization occurring in the high density models during the deflagration phase yields ^{56}Ni massest hat are more or less constant with ρ_c for the brighter SNe. Only dim SNe, which have a strong deflagration phase and expansion prior to the DDT, exhibit a trend of decreasing ^{56}Ni mass with increasing density, since the increased neutronization in the deflagration phase cannot be compensated for by the relatively weak detonation phase. This trend, however, is of secondary importance when compared to the effects of varying the ignition kernel distribution. For a given ignition kernel spatial distribution, the central density therefore influences the brightness of the supernova event only as a secondary parameter. From the works of Townsley et al. (2009) and Bravo et al. (2010), it appears that the same holds for composition, i.e. metallicity and C/O ratio. Indeed, based on an analysis of high-quality V and B-band light curves of SNe Ia from the Carnegie Supernova Project, Höflich et al. (2010) propose that the composition and central density are two independent secondary parameters for SN Ia light curves. In light of the importance of the ignition configuration of the deflagration for the brightness of the SN, it is most crucial to establish how the central density at ignition (cooling time) and metallicity affect the statistical properties (notably number and location) of the ignition sparks themselves, and not their respective direct effects on the outcome of an explosion once a random ignition spark distribution was chosen. One should therefore aim to quantify which effect composition, cooling and accretion history have on the ignition process, for example by mapping them into the exponentiation parameter C_e of the stochastic ignition prescription of Schmidt & Niemeyer (2006c). This would require a better understanding of the physics leading up to ignition, including the nature of the convection and effects of electron captures and the convective URCA process.

ACKNOWLEDGEMENTS

The simulations presented here were carried out as part of the DEISA grant "SN-DET-hires" on facilities of the Leibnitz Rechenzentrum, in part on the JUGENE supercomputer at the Forschungszentrum Jülich within project HMU13, and in part at the Computer Center of the Max Planck Society, Garching, Germany. This work was supported by the Deutsche Forschungsgemeinschaft via the Transregional Collaborative Research Center TRR 33 "The Dark Universe", the Emmy Noether Program (RO 3676/1-1), and the Excellence Cluster EXC 153. We also want to thank Wolfgang Hillebrandt for reading the manuscript and his helpful comments.

REFERENCES

Albrecht A., Bernstein G., Cahn R., Freedman W. L., Hewitt J., Hu W., Huth J., Kamionkowski M., Kolb E. W., Knox L., Mather J. C., Staggs S., Suntzeff N. B., 2006, ArXiv Astrophysics e-prints

Arnett D., Livne E., 1994, ApJ, 427, 330

Blinnikov S. I., Khokhlov A. M., 1986, Soviet Astronomy Letters, 12, 131

Blondin S., Mandel K. S., Kirshner R. P., 2011, A&A, 526, A81+

Bravo E., Domínguez I., Badenes C., Piersanti L., Straniero O., 2010, ApJ, 711, L66

Bravo E., García-Senz D., 2008, A&A, 478, 843

Cameron A. G. W., 1959, ApJ, 130, 916

Chan K.-W., Lingenfelter R. E., 1993, ApJ, 405, 614

Ciaraldi-Schoolmann F., Schmidt W., Niemeyer J. C., Röpke F. K., Hillebrandt W., 2009, ApJ, 696, 1491

Colella P., Woodward P. R., 1984, Journal of Computational Physics, 54, 174

Contardo G., Leibundgut B., Vacca W. D., 2000, A&A, 359, 876

Cooper R. L., Steiner A. W., Brown E. F., 2009, ApJ, 702, 660
Fink M., Röpke F. K., Hillebrandt W., Seitenzahl I. R., Sim S. A., Kromer M., 2010, A&A, 514, A53+
Fryxell B. A., Müller E., Arnett W. D., 1989, MPA Green Report 449, Hydrodynamics and nuclear burning. Max-Planck-Institut für Astrophysik, Garching
Gallagher J. S., Garnavich P. M., Caldwell N., Kirshner R. P., Jha S. W., Li W., Ganeshalingam M., Filippenko A. V., 2008, ApJ, 685, 752
Gamezo V. N., Khokhlov A. M., Oran E. S., 2005, ApJ, 623, 337
García-Senz D., Bravo E., 2005, A&A, 430, 585
Gasques L. R., Afanasjev A. V., Aguilera E. F., Beard M., Chamon L. C., Ring P., Wiescher M., Yakovlev D. G., 2005, Phys. Rev. C, 72, 025806
Gasques L. R., Brown E. F., Chieffi A., Jiang C. L., Limongi M., Rolfs C., Wiescher M., Yakovlev D. G., 2007, Phys. Rev. C, 76, 035802
Golombek I., Niemeyer J. C., 2005, A&A, 438, 611
Höflich P., Krisciunas K., Khokhlov A. M., Baron E., Folatelli G., Hamuy M., Phillips M. M., Suntzeff N., Wang L., NSF07-SNIa Collaboration 2010, ApJ, 710, 444
Höflich P., Stein J., 2002, ApJ, 568, 779
Hoyle F., Fowler W. A., 1960, ApJ, 132, 565
Iapichino L., Lesaffre P., 2010, A&A, 512, A27+
Itoh N., Tomizawa N., Wanajo S., Nozawa S., 2003, ApJ, 586, 1436
Jackson A. P., Calder A. C., Townsley D. M., Chamulak D. A., Brown E. F., Timmes F. X., 2010, ApJ, 720, 99
Jiang C. L., Rehm K. E., Back B. B., Janssens R. V. F., 2007, Phys. Rev. C, 75, 015803
Kasen D., Röpke F. K., Woosley S. E., 2009, Nature, 460, 869
Kerstein A. R., 1988, Combust. Sci. Technol., 60, 441
Khokhlov A. M., 1991a, A&A, 245, 114
Khokhlov A. M., 1991b, A&A, 246, 383
Khokhlov A. M., 1995, ApJ, 449, 695
Khokhlov A. M., Oran E. S., Wheeler J. C., 1997, ApJ, 478, 678
Krueger B. K., Jackson A. P., Townsley D. M., Calder A. C., Brown E. F., Timmes F. X., 2010, ApJ, 719, L5
Kuhlen M., Woosley S. E., Glatzmaier G. A., 2006, ApJ, 640, 407
Langanke K., Martínez-Pinedo G., 2001, Atomic Data and Nuclear Data Tables, 79, 1
Lesaffre P., Han Z., Tout C. A., Podsiadlowski P., Martin R. G., 2006, MNRAS, 368, 187
Lisewski A. M., Hillebrandt W., Woosley S. E., 2000, ApJ, 538, 831
Livne E., 1999, ApJ, 527, L97
Livne E., Asida S. M., Höflich P., 2005, ApJ, 632, 443
Matteucci F., Greggio L., 1986, A&A, 154, 279
Meakin C. A., Seitenzahl I., Townsley D., Jordan G. C., Truran J., Lamb D., 2009, ApJ, 693, 1188
Miknaitis G. et al., 2007, ApJ, 666, 674
Niemeyer J. C., Woosley S. E., 1997, ApJ, 475, 740
Osher S., Sethian J. A., 1988, Journal of Computational Physics, 79, 12
Piro A. L., Bildsten L., 2008, ApJ, 673, 1009
Piro A. L., Chang P., 2008, ApJ, 678, 1158
Reinecke M., Hillebrandt W., Niemeyer J. C., Klein R., Gröbl A., 1999, A&A, 347, 724
Riess A. G. et al., 1998, AJ, 116, 1009
Röpke F. K., 2005, A&A, 432, 969
Röpke F. K., 2007, ApJ, 668, 1103
Röpke F. K., Gieseler M., Reinecke M., Travaglio C., Hillebrandt W., 2006, A&A, 453, 203
Röpke F. K., Hillebrandt W., 2005a, A&A, 429, L29
Röpke F. K., Hillebrandt W., 2005b, A&A, 431, 635
Röpke F. K., Hillebrandt W., Niemeyer J. C., Woosley S. E., 2006, A&A, 448, 1
Röpke F. K., Hillebrandt W., Schmidt W., Niemeyer J. C., Blinnikov S. I., Mazzali P. A., 2007, ApJ, 668, 1132
Röpke F. K., Niemeyer J. C., 2007, A&A, 464, 683
Röpke F. K., Woosley S. E., Hillebrandt W., 2007, ApJ, 660, 1344
Scannapieco C., Tissera P. B., White S. D. M., Springel V., 2008, MNRAS, 389, 1137
Schmidt B. P. et al., 1998, ApJ, 507, 46
Schmidt W., Niemeyer J. C., Hillebrandt W., 2006a, A&A, 450, 265
Schmidt W., Niemeyer J. C., Hillebrandt W., Röpke F. K., 2006b, A&A, 450, 283
Schmidt W., Niemeyer J. C., 2006c, A&A, 446, 627
Seitenzahl I. R., Townsley D. M., Peng F., Truran J. W., 2009, Atomic Data and Nuclear Data Tables, 95, 96
Smiljanovski V., Moser V., Klein R., 1997, Combustion Theory Modelling, 1, 183
Sreenivasan K. R., 1991, Annual Review of Fluid Mechanics, 23, 539
Stritzinger M., Leibundgut B., Walch S., Contardo G., 2006a, A&A, 450, 241
Stritzinger M., Mazzali P. A., Sollerman J., Benetti S., 2006b, A&A, 460, 793
Timmes F. X., Brown E. F., Truran J. W., 2003, ApJ, 590, L83
Townsley D. M., Jackson A. P., Calder A. C., Chamulak D. A., Brown E. F., Timmes F. X., 2009, ApJ, 701, 1582
Travaglio C., Hillebrandt W., Reinecke M., 2005, A&A, 443, 1007
Wood-Vasey W. M. et al., 2007, ApJ, 666, 694
Woosley S. E., 1990, in Petschek A. G., ed., Supernovae Type Ia supernovae: Carbon deflagration and detonation. Springer-Verlag, New York, pp 182–212
Woosley S. E., 1997, in P. Ruiz-Lapuente, R. Canal, & J. Isern ed., NATO ASIC Proc. 486: Thermonuclear Supernovae Type ia supernovae: flame physics and models. pp 313–+
Woosley S. E., 2007, ApJ, 668, 1109
Woosley S. E., Kerstein A. R., Sankaran V., Aspden A. J., Röpke F. K., 2009, ApJ, 704, 255
Woosley S. E., Wunsch S., Kuhlen M., 2004, ApJ, 607, 921
Wunsch S., Woosley S. E., 2004, ApJ, 616, 1102
Zel'dovich Y. B., Librovich V. B., Makhviladze G. M., Sivashinskii G. I., 1970, Journal of Applied Mechanics and Technical Physics, 11, 264
Zhang J., Messer O. E. B., Khokhlov A. M., Plewa T., 2007, ApJ, 656, 347
Zingale M., Almgren A. S., Bell J. B., Nonaka A., Woosley S. E., 2009, ApJ, 704, 196